

A Hermite-like basis for faster matrix-free evaluation of interior penalty discontinuous Galerkin operators*

Martin Kronbichler[†] Katharina Kormann[‡] Niklas Fehn[†] Peter Munch^{†§}
 Julius Witte[¶]

July 22, 2019

Abstract

This work proposes a basis for improved throughput of matrix-free evaluation of discontinuous Galerkin symmetric interior penalty discretizations on hexahedral elements. The basis relies on ideas of Hermite polynomials. It is used in a fully discontinuous setting not for higher order continuity but to minimize the effective stencil width, namely to limit the neighbor access of an element to one data point for the function value and one for the derivative. The basis is extended to higher orders with nodal contributions derived from roots of Jacobi polynomials and extended to multiple dimensions with tensor products, which enable the use of sum factorization. The beneficial effect of the reduced data access on modern processors is shown. Furthermore, the viability of the basis in the context of multigrid solvers is analyzed. While a plain point-Jacobi approach is less efficient than with the best nodal polynomials, a basis change via sum-factorization techniques enables the combination of the fast matrix-vector products with effective multigrid constituents. The basis change is essentially for free on modern hardware because these computations can be hidden behind the cost of the data access.

Key words. High-order discontinuous Galerkin, matrix-free method, sum factorization, high-performance computing, multigrid method.

1 Introduction

High-order discontinuous Galerkin (DG) methods, traditionally most popular for conservation laws, are gaining in popularity also for elliptic problems. For example, representing the pressure Poisson equation in incompressible flows with discontinuous pressure spaces combines naturally with $H(\text{div})$ conforming velocity spaces [30] (e.g., Raviart–Thomas spaces in the case of hexahedral elements) or stabilized DG spaces [14, 36]. In the context of solving linear systems, DG methods are often considered expensive due to a relatively wide stencil, because each shape function is densely coupled to all the shape functions within a cell as well as to the neighbors. In primal formulations of elliptic operators, such as the interior penalty method for the scalar Poisson equation considered in this

*This work was supported by the German Research Foundation (DFG) under the project “High-order discontinuous Galerkin for the exa-scale” (ExaDG) within the priority program “Software for Exascale Computing” (SPPEXA), grant agreement no. KO5206/1-1 and KR4661/2-1, as well as the Bayerische Kompetenznetzwerk für Technisch-Wissenschaftliches Hoch- und Höchstleistungsrechnen (KONWIHR) in the framework of the project “Performance tuning of high-order discontinuous Galerkin solvers for SuperMUC-NG”. The authors gratefully acknowledge the Gauss Centre for Supercomputing e.V. (www.gauss-centre.eu) for funding this project by providing computing time on the GCS Supercomputer SuperMUC at Leibniz Supercomputing Centre (LRZ, www.lrz.de) through project id pr83te.

[†]Institute for Computational Mechanics, Technical University of Munich, Boltzmannstr. 15, 85748 Garching, Germany ([{kronbichler, fehn, munch}@lrm.tum.de">kronbichler, fehn, munch}@lrm.tum.de](mailto)).

[‡]Max Planck Institute for Plasma Physics, Boltzmannstr. 2, 85748 Garching, Germany (katharina.kormann@ipp.mpg.de).

[§]Institute of Materials Research, Materials Mechanics, Helmholtz-Zentrum Geesthacht, Max-Planck-Str. 1, 21502 Geesthacht, Germany (peter.muench@hzg.de).

[¶]Interdisciplinary Center for Scientific Computing, Heidelberg University, Im Neuenheimer Feld 205, 69120 Heidelberg, Germany (julius.witte@iwr.uni-heidelberg.de).

work, the neighbor coupling links to all shape functions which have a non-zero value or non-zero first derivative on the face. This corresponds to all unknowns on the neighboring elements for conventional bases. For tensor product shape functions, the polynomial space is also much larger than necessary to describe the complete polynomial space of degree p . In order to reduce the memory requirements and memory transfer of matrix-based approaches, more compact schemes like the compact discontinuous Galerkin method [34], the hybridizable discontinuous Galerkin method [9], or the line discontinuous Galerkin method [35] have been developed. Also, finite element bases with reduced sparsity within an element have been proposed [7].

An alternative path to more efficient DG solvers are matrix-free implementations, using ideas originally developed within spectral elements [11, 24, 33]. Rather than assembling a global sparse matrix that is later used in some iterative linear solver, these methods compute the matrix-vector product in terms of the underlying integrals on the fly by fast quadrature. These matrix-free methods allow to use the tensor product (Kronecker) structure in the shape functions and the quadrature points: For interpolation between solution coefficients and values or derivatives at quadrature points, the so-called sum-factorization approach separates the interpolation along each of the coordinate directions from the constant factors in the other directions, thereby reaching a complexity of $\mathcal{O}(p^{d+1})$ arithmetic operations per cell in the polynomial degree p in d dimensions for the interpolation. Scaled to the number of operations per degree of freedom, the cost is linear, $\mathcal{O}(p)$. The observed throughput of operator evaluation with sum-factorization schemes is often constant per degree of freedom for moderately high polynomial degrees $p \leq 10$ when face integrals and memory access of complexity $\mathcal{O}(p^d)$ dominate over the $\mathcal{O}(p^{d+1})$ complexity of cell integrals [15]. Even better, when executed on modern memory-bandwidth-starved hardware, matrix-free operator evaluation for polynomial degrees $3 \leq p \leq 10$ is also several times faster than a sparse matrix-vector product for *continuous linear* finite elements with the same number of unknowns [29]. Furthermore, the final matrix entries do not possess a tensor product structure for variable coefficients or deformed elements and thus the sparse matrix-vector product involves $\mathcal{O}(p^d)$ operations per unknown.

While fast operator evaluation is well-established in explicit time integration, iterative solvers are often preconditioned by schemes such as the Gauss–Seidel relaxation or incomplete factorizations, which explicitly rely on the matrix entries and are not compatible with integration-based matrix-free methods. For multigrid schemes, selected smoothers such as a Chebyshev iteration around the Jacobi method [1, 39] or methods based on the fast diagonalization method [31] enable optimal $\mathcal{O}(1)$ storage complexity per unknown and ensure that the matrix-vector product dominates. Apart from the serial performance, they are particularly interesting in a parallel setting. We note that the application metric driving the present work is time to solution, given by the number of effective iterations (matrix-vector products) times the cost of a matrix-vector product as discussed in [13].

Regarding the efficiency of matrix-free methods, DG spectral-element methods (DGSEM) with collocated node points for Lagrange polynomials and integration points have been most popular [24]. For DG methods, one can choose between nodal polynomials in the points of Gauss–Lobatto polynomials and in the points of the Gauss quadrature. While the latter ensures exact integration on affine geometries, the former has nodes at the boundary which simplifies access to values on faces, at the price of additional discretization errors due to the Gauss–Lobatto quadrature.

Progress in computer hardware has made computations cheaper relative to data movement. As a consequence, the data access patterns are as important as the number of arithmetic operations in the selection of a basis, as has been found in a recent study [37]. This is because matrix-free operator evaluation with a state-of-the-art implementation, like the one from the deal.II finite element library [3] used in this work, comes close to the throughput of simply streaming the input and output vectors on modern processors. Computer architecture therefore fosters a data-centric point of view with the goal to reduce the memory transfer to a minimum when traversing through the grid, an optimization technique well-known from high-performance finite difference implementations [18]. The present work meets these requirements by proposing a Hermite-like basis compatible with a single sweep through data for both cell and face integrals with minimal data access for the prototype second-derivative DG operator, the symmetric interior penalty method. The selection of this type of shape functions is orthogonal to the typical use of Hermite polynomials in the context of continuous finite elements for reaching higher order of regularity (e.g. C^1 continuity), see also a

recent work on wave propagation [4]. Instead, we keep a fully discontinuous L_2 -conforming ansatz space similar to the work by [19]. The chosen basis covers the same function space as a nodal Lagrange basis and is integrated with the same Gaussian quadrature producing exact integrals on affine element shapes, and, therefore, does not alter accuracy.

This work is structured as follows. The DG discretization is introduced in section 2 and the chosen matrix-free implementation in section 3. The Hermite-like basis functions with well-conditioned interpolation are constructed in section 4. Section 5 gives an in-depth performance analysis of the matrix-free operator evaluation with the new basis against established approaches, supported by a cache analysis. In section 6 an efficient multigrid scheme with this method is discussed before conclusions are given in section 7.

2 Discontinuous Galerkin discretization of the Laplacian

We consider the symmetric interior penalty discretization of the scalar Laplacian according to [5], whose homogeneous part on an element K is given by the weak form

$$(\nabla\varphi_i, \nabla u_h)_K + \sum_{F \in \text{faces}(K)} \langle \varphi_i \hat{n}, \sigma \llbracket u_h \rrbracket \rangle_F - \langle \varphi_i \hat{n}, \{\{ \nabla u_h \} \} \rangle_F - \left\langle \frac{\nabla \varphi_i}{2}, \llbracket u_h \rrbracket \right\rangle_F, \quad (1)$$

where $u_h = \sum_j \varphi_j u_j$ is the finite element interpolation based on shape functions φ_j and the vector entries u_j . In equation (1), the operator $\{\{v\}\} = \frac{v^- + v^+}{2}$ denotes the average of the quantity v over a face from the interior value v^- on the cell K and the value u^+ on the neighbor K^+ behind the respective face, and $\llbracket v \rrbracket = \hat{n}^- v^- + \hat{n}^+ v^+ = \hat{n}(v^- - v^+)$ the directed jump over the interface along the direction of the outer normal $\hat{n} = \hat{n}^-$ of cell K . The parameter σ is a penalty parameter chosen large enough in terms of the polynomial degree p and the mesh size h to make the final weak form coercive, $\sigma = (p+1)^2/h$, see e.g. [12]. The bilinear forms $(\cdot, \cdot)_K$ and $\langle \cdot, \cdot \rangle_F$ denote the integration of the product of the two arguments over the cell K and on the face F , respectively. Boundary conditions are assumed to be implemented via the mirror principle, e.g., $u^+ = -u^-$ on homogeneous Dirichlet boundaries.

In this work, we consider high-order DG methods on a mesh of hexahedral elements where sum factorization is most straight-forward. In reference coordinates, the basis functions

$$\varphi_i(\boldsymbol{\xi}) = \phi_{i_1}(\xi_1) \phi_{i_2}(\xi_2) \dots \phi_{i_d}(\xi_d) \quad (2)$$

are constructed as the tensor product of one-dimensional polynomials ϕ in each of the d coordinate directions. For polynomial degree p , this results in $(p+1)^d$ basis functions per element. In the usual finite element setting, the functions in real space \boldsymbol{x} are defined by a transformation from a reference space $\boldsymbol{\xi} \in [0, 1]^d$ to the real space using some polynomial mapping. In the DG method, no continuity over the element faces is imposed. The terms in (1) are tested by all test functions φ_i , $i = 1, \dots, (p+1)^d$, and for all elements K in the mesh, resulting in a linear system with $n_{\text{DoF}} = n_{\text{elements}}(p+1)^d$ global equations and unknowns.

3 Matrix-free evaluation of finite element operators

In matrix-free operator evaluation, the matrix-vector product $\boldsymbol{y} = \boldsymbol{A}\boldsymbol{u}$ is evaluated in terms of the weak form (1) using the finite element field u_h associated with the vector values in \boldsymbol{u} . The integrals are computed by quadrature on n_q^d Gauss quadrature points. On affine geometries and for constant coefficients, choosing $n_q = p+1$ quadrature points ensures exact integration. For variable coefficients, nonlinear terms, or curved geometries, $n_q > p+1$ is sometimes needed for accurate results. For the example of the cell term $(\nabla\varphi_i, \nabla u_h)_K$, the integral is approximated by

$$\begin{aligned} (\nabla\varphi_i, \nabla u_h)_K &= \int_{\Omega_{\text{unit}}} (\mathcal{J}_K^{-\top} \nabla_{\boldsymbol{\xi}} \varphi_i)^\top \left(\mathcal{J}_K^{-\top} \sum_{j=1}^{(p+1)^d} \nabla_{\boldsymbol{\xi}} \varphi_j u_j^{(K)} \right) \det(\mathcal{J}_K) \, d\boldsymbol{\xi} \\ &\approx \sum_{q=1}^{n_q^d} (\nabla_{\boldsymbol{\xi}} \varphi_i(\boldsymbol{\xi}_q))^\top \underbrace{\mathcal{J}_K^{-1} \mathcal{J}_K^{-\top} \det(\mathcal{J}_K)}_{\text{depends only on q-point}} w_q \sum_{j=1}^{(p+1)^d} \nabla_{\boldsymbol{\xi}} \varphi_j(\boldsymbol{\xi}_q) u_j^{(K)}. \end{aligned} \quad (3)$$

Here, \mathcal{J}_K denotes the Jacobian of the mapping from the reference to the real cell at the quadrature points and w_q the quadrature weight. Since the metric terms do not depend on the shape function indices i and j , they are evaluated outside the i and j loops, a common abstraction in matrix-free methods [15, 23, 25, 26].

In this version of the algorithm, the work at quadrature points is of complexity $\mathcal{O}(n_q^d)$, whereas the interpolation sum over j as well as testing by all test functions φ_i would both imply a cost of $\mathcal{O}((p+1)^d n_q^d)$ per element. The interpolation is amenable to BLAS-3 linear algebra because the same reference-element operations is applied on each element K . Furthermore, the interpolation and derivative matrices have more structure in case the polynomials are the tensor product of 1D polynomials according to (2) and integrated with a tensor product quadrature formula: The two nested loops over $(p+1)^d$ basis functions and n_q^d points can be broken down into a series of smaller loops along each of the coordinate directions by a technique called sum factorization [11, 24]. The overall complexity per element is then $\mathcal{O}(p^{d+1})$ for $n_q \sim p$.

Let us denote by $S = S_{q,j}$ the $n_q \times (p+1)$ matrix of all 1D shape functions ϕ_j evaluated at all 1D quadrature points ξ_q and by $D = D_{q,j}$ the derivative of the shape functions $\phi_j^{\text{1D,co}}(\xi_q)$ with nodes in the quadrature points evaluated at ξ_q (collocation basis). Then, the sum over j evaluated at all quadrature points in (3) can be written in matrix-vector notation as

$$\begin{bmatrix} \partial \mathbf{u}_h / \partial \xi_1 \\ \partial \mathbf{u}_h / \partial \xi_2 \\ \vdots \\ \partial \mathbf{u}_h / \partial \xi_d \end{bmatrix} = \begin{bmatrix} I \otimes \dots \otimes I \otimes D \\ I \otimes \dots \otimes D \otimes I \\ \vdots \\ D \otimes I \otimes \dots \otimes I \end{bmatrix} [S \otimes \dots \otimes S \otimes S] \mathbf{u}^{(K)}. \quad (4)$$

The first multiplication $[S \otimes S \otimes \dots \otimes S] \mathbf{u}^{(K)}$ is a basis change, going from the values $\mathbf{u}^{(K)}$ in the solution vector to a representation in the nodal basis of Lagrange polynomials defined in the quadrature points. The gradient operation is then performed in this basis. In equation (4), the evaluation of the matrices in Kronecker product form is understood by the usual 1D contractions along each dimension with sum factorization, which amounts to $2d$ products for the complete gradient (4), see [15, 26] and references therein. The integration step involves the transpose of the matrix from (4).

Analogously, the evaluation of the face integrals of equation (1) involves reference-cell operations from both sides of a face, as well as geometrical and equation-dependent operations at quadrature points. For a face with normal vector in negative ξ_1 direction in three dimensions, the interpolation is given by

$$\begin{bmatrix} \mathbf{u}_h \\ \partial \mathbf{u}_h / \partial \xi_2 \\ \partial \mathbf{u}_h / \partial \xi_3 \\ \partial \mathbf{u}_h / \partial \xi_1 \end{bmatrix} = \begin{bmatrix} \left[\begin{array}{c} I \otimes I \\ I \otimes D \\ D \otimes I \end{array} \right] [S \otimes S] & 0 \\ 0 & [S \otimes S] \end{bmatrix} \begin{bmatrix} I \otimes I \otimes S_f \\ I \otimes I \otimes D_f \end{bmatrix} \mathbf{u}^{(K)}, \quad (5)$$

where the $(p+1) \times 1$ matrix S_f contains the values of all shape functions ϕ_i at $\xi = 0$, and the $(p+1) \times 1$ matrix D_f contains the evaluation of the first derivative of all shape functions ϕ'_i at $\xi = 0$. Note that this operation returns four vectors of length n_q^2 , representing the values $u_h(\xi_q)$ and the three components of the gradient $\nabla_{\xi} u_h(\xi_q)$ in reference coordinates. Similar operations can be defined for the other faces and, in transposed form, for integration. The key observation for face integrals is that the initial multiplications by the matrices S_f and D_f extract the degrees of freedom relevant for face integrals from the solution vector $\mathbf{u}^{(K)}$. Entries where both S_f and D_f are zero need not be loaded, independent of the geometry. As proposed in [26], interpolation operations on interior faces can share some basis change operations with the cell integrals, such that the full interpolation according to equation (5) is only necessary on the neighbors' face data u_h^+ .

In terms of the arrangement of cell and face integrals, we concentrate on an algorithm that is referred to as an ‘‘element-wise evaluation of face integrals’’ in [26]. Here, all integrals related to an element K (or to a batch of elements when vectorizing over several elements) are computed together. This enables a single write operation to the result vector with a single sweep through the vector and thus minimizes the data movement. At the same time, this setup evaluates the flux on interior faces twice. For a comparison to other arrangements of face integrals and their properties, we refer to [26, Sec. 4.6].

In this work, we assume that the geometry terms \mathcal{J} are possibly space-varying, necessitating separate interpolation and integration steps with all cross-terms in the derivatives. If \mathcal{J} were

constant within an element, i.e., a cell subject to an affine transformation, the integration could be completed in reference coordinates and the full interpolation and integration step could be expressed by a sum of a few Kronecker matrices, reducing the number of arithmetic operations especially on faces. We do not consider those optimizations in this work because pre-computed Kronecker matrices would allow for further algorithmic rearrangements such as element-wise static condensation [21], and are not applicable to variable geometries for which DG methods have been originally developed.

4 Hermite-like basis functions

The selection of the basis in DG methods is more relaxed as compared with continuous finite elements where inter-element continuity is imposed by shared nodes. The following three principles can be applied:

- a modal basis where the final mass matrix is diagonal to ensure cheap explicit time integration, see e.g. [10], also easily separating low/high frequency content,
- a basis where the transformation S is the identity matrix, i.e., a nodal basis with the nodes coinciding with the points of the quadrature formula, the typical spectral element/DGSEM setup [20, 24], or
- a basis where the number of entries in S_f and D_f is explicitly minimized.

The collocation setup with $S = I$ and $n_q = p + 1$ Gaussian quadrature points is widely used and simplifies several operations in both the cell integrals of equation (4) as well as face integrals of equation (5). Furthermore, it also implies a diagonal mass matrix. However, for Gaussian quadrature all entries in S_f and D_f are non-zero because all roots of the underlying Legendre polynomials are strictly inside the 1D reference element. When switching to the less accurate collocated Gauss–Lobatto quadrature, $S_f = [1, 0, \dots, 0]$ becomes simple, but D_f is still dense. Furthermore, as soon as over-integration with $n_q > p + 1$ is used, the identity $S = I$ is lost and all matrices in the formulas (4) and (5) must be used.

4.1 Construction of the basis

In this work, we minimize the access into \mathbf{u} for face integrals, i.e., maximize the number of columns where both the matrices S_f and D_f have zero entries. More precisely, the idea is to generalize the favorable access pattern of Lagrange polynomials in the Gauss–Lobatto points for hyperbolic problems, where solution values on faces access only $(p + 1)^{d-1}$ entries due to $S_f = [1, 0, \dots, 0]$, to settings where values and gradients are needed on faces. In the recent analysis [37] it has been shown that a tight data access via $S_f = [1, 0, \dots, 0]$ outweighs the additional calculations with dense matrices S on modern hardware. With respect to minimizing the number of nonzeros in D_f , it is necessary to make the first derivative vanish at $\xi = 0$ and $\xi = 1$ for all shape functions but one, naturally leading to the Hermite basis for $p = 3$ with

$$D_f = [0, 1, 0, \dots, 0]. \quad (6)$$

The four cubic Hermite polynomials—shown in Figure 1 (left)—are defined as

$$\phi_0^H(\xi) = 2\xi^3 - 3\xi^2 + 1, \quad \phi_1^H(\xi) = \xi^3 - 2\xi^2 + \xi, \quad \phi_2^H(\xi) = \xi^3 - \xi^2, \quad \phi_3^H(\xi) = -2\xi^3 + 3\xi^2. \quad (7)$$

Regarding the case $p > 3$, the support of higher derivatives on the reference cell boundary can be limited, which leads to the Bernstein–Bézier polynomial basis. While this basis has attractive properties such as a fast recursive evaluation of polynomials or applicability of sum factorization algorithms also for triangular and tetrahedral elements [2] including inverse mass matrices [22], the exponential increase in the condition number requires careful algorithm selection to not spoil the attractive properties by roundoff effects. Hermite-type polynomials have already been considered in the DG context for constructing better multigrid smoothers in [19].

If we limit ourselves to minimizing the entries of S_f and D_f , higher order polynomials can be constructed via

$$\phi_i^{(p)}(\xi) = 16\xi^2(1 - \xi)^2\sigma_i^{(p)}(\xi), \quad (8)$$

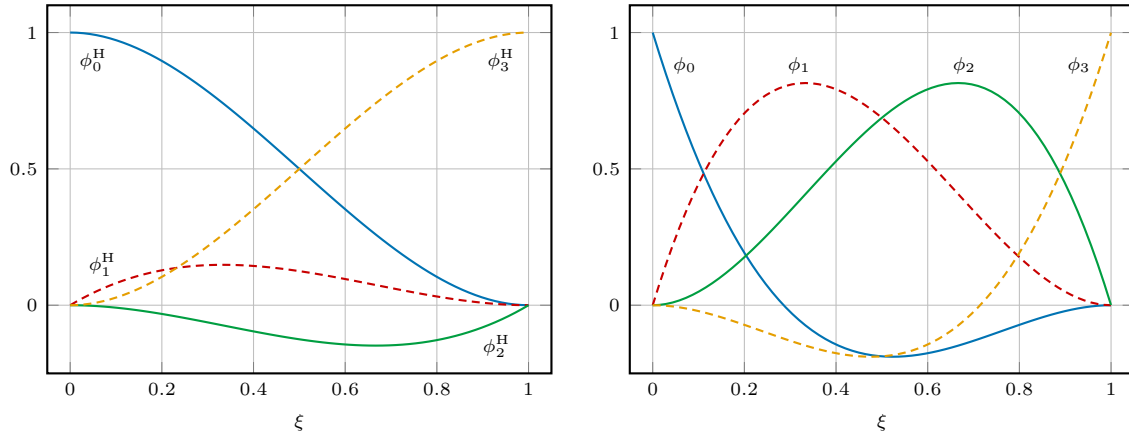


Figure 1: Classical Hermite basis functions (7) (left) and proposed Hermite-like basis functions (right) for degree $p = 3$.

Table 1: Condition number of the 1D mass matrix for the Hermite interpolation extended by Legendre polynomials in (8) and for the proposed Hermite-like interpolation. The condition number of the standard nodal Lagrange basis on the Gauss-Lobatto points is included for reference.

p	Hermite + Legendre extension	Hermite-like basis	Lagrange basis on GL points
3	$1.06 \cdot 10^3$	17.2	8.65
4	$6.58 \cdot 10^3$	16.8	10.4
5	$1.88 \cdot 10^4$	16.0	12.0
6	$6.03 \cdot 10^4$	16.3	13.6
7	$1.28 \cdot 10^5$	17.1	15.2
8	$2.85 \cdot 10^5$	18.2	16.7
10	$9.76 \cdot 10^5$	20.7	19.9
15	$9.43 \cdot 10^6$	27.9	27.7
20	$5.67 \cdot 10^7$	35.7	35.5
25	$2.22 \cdot 10^8$	43.5	43.4
30	$7.73 \cdot 10^8$	51.6	51.2

where $\sigma_i^{(p)}(\xi)$ with $i = 4, \dots, p$ is a polynomial of degree up to $p - 4$. These polynomials are bubble functions with vanishing values and first derivatives on both faces. A naive possibility is to choose Legendre polynomials. Table 1 lists the quality of this basis measured by the condition number of the 1D consistent mass matrix. The condition number is 10^3 already for the cubic Hermite case $p = 3$ and further deteriorates as the degree increases.

In order to improve the conditioning of interpolation, we relax the Hermite polynomials into a basis we call ‘‘Hermite-like’’, illustrated in Figures 1 and 2. The construction of the basis is as follows:

- 1. Relaxation to two nonzero entries in D_f for improved conditioning.** In order to improve conditioning with $p = 3$, we relax the polynomial ϕ_0^H by allowing $\phi_0'(0) \neq 0$ via a free root ξ_1 in the form $\phi_0(\xi) = \alpha_0(\xi - \xi_1)(\xi - 1)^2$ with some constant α_0 . Furthermore, we set $\phi_1(\xi) = \alpha_1\xi(\xi - 1)^2$ with some constant α_1 . The root ξ_1 is fixed by the heuristic argument that the orthogonality between ϕ_0 and ϕ_1 , $\int_0^1 \phi_0\phi_1 d\xi = 0$, will keep the condition number low. For $p = 3$, we obtain $\xi_1 = \frac{2}{7}$. The requirement $\phi_0(0) = 1$ then gives $\alpha_0 = -\frac{1}{\xi_1} = -\frac{7}{2}$. The second constant α_1 is determined by the condition $\phi_1'(0) = -\phi_0'(0)$, which gives a relaxed condition

$$D_f = [-\alpha_1, \alpha_1, 0, \dots, 0]. \quad (9)$$

The constant evaluates to $\alpha_1 = \frac{2\xi_1+1}{\xi_1} = \frac{11}{2}$. The polynomials ϕ_2 and ϕ_3 are obtained by mirroring ϕ_1 and ϕ_0 at $\xi = \frac{1}{2}$.

Note that relaxing D_f to two non-zero entries does not worsen data access because the first entry of S_f is nonzero anyway and equations which only need the derivative on faces are uncommon. More importantly, any non-Cartesian element shape must evaluate tangential

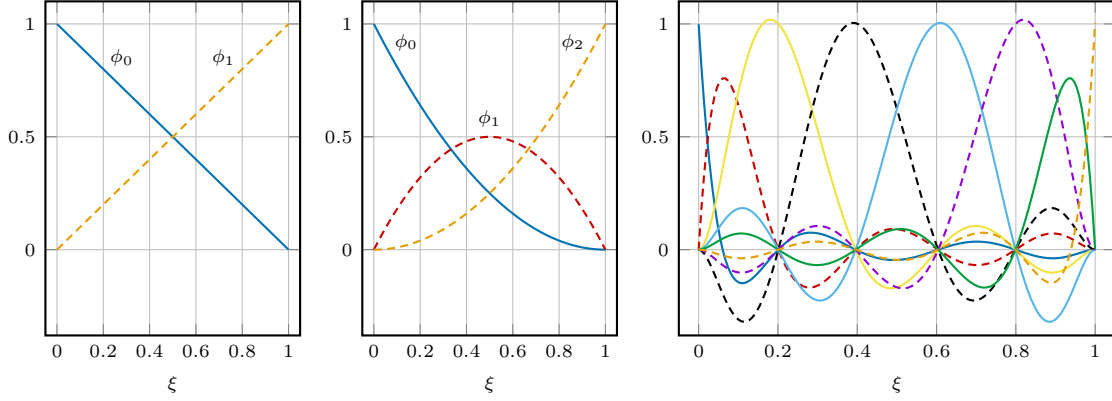


Figure 2: Hermite-like basis for $p = 1$ (left), $p = 2$ (middle), and $p = 7$ (right).

derivatives in reference space as well, for which the values on the face are needed. For evaluating only the values on a face, e.g. for a hyperbolic term, a single value is touched via S_f .

2. **Construction for $p \leq 2$.** We require $D^f = [-\alpha_1, \alpha_1, 0]$ at $\xi = 0$ and $D^f = [0, -\alpha_1, \alpha_1]$ at $\xi = 1$ with $\alpha_1 = 2$ for $p = 2$, see Figure 2 and Appendix A. For $p = 1$, the standard Lagrange basis $\{1 - \xi, \xi\}$ satisfies $S^f = [1, 0]$ and (9).
3. **Extension for $p > 3$.**

- (a) Higher order polynomials are defined in a nodal way, placing additional nodes within the reference element. To ensure robust conditioning for large p , the nodes are specified as the roots of the Jacobi polynomial $P_{p-3}^{4,4}$, i.e., the Jacobi polynomials orthogonal with respect to the function $\xi^4(1-\xi)^4$, see also [19]. This ensures L_2 orthogonality between the bubble functions (8). Note that we define the reference interval to be $(0, 1)$ in this work.
- (b) The four polynomials active at the boundaries are of degree p with factors $\xi - \xi_l$ involving the $p - 3$ roots of $P_{p-3}^{4,4}$, plus the boundary contribution $\alpha_0(\xi - \xi_1)(\xi - 1)^2$ for ϕ_0 , for instance. The additional root ξ_1 is determined by the orthogonality between ϕ_0 and ϕ_1 . Since the two polynomials ϕ_0 and ϕ_1 only differ by a constant and the factor $\xi - \xi_1$ or ξ , respectively, the equation for ξ_1 is linear that is easily solved.
- (c) The weights α_0 and α_1 of ϕ_0, ϕ_1 are determined by $\phi_0(0) = 1$, i.e., $S_f = [1, 0, \dots, 0]$, and $\phi_0'(0) = -\phi_1'(0)$, i.e., relation (9). This makes sure that the function of all ones, $\mathbf{u} = [1, 1, \dots, 1]^T$, represents the constant function $u_h \equiv 1$.

The condition number of the mass matrix resulting from the Hermite-like basis in Table 1 shows a linear increase with the polynomial degree, in analogy to the condition number for the standard Lagrange basis defined in the points of the Gauss–Lobatto quadrature formula. The proposed construction makes the polynomial basis symmetric with respect to the center of the reference element $\xi = \frac{1}{2}$ in the sense $\phi_i(\xi) = \phi_{p-i}(1 - \xi)$ for $i = 0, \dots, p$ like a Lagrange basis. This enables to straight-forwardly apply optimizations for nodal bases such as the even-odd decomposition that cuts the work of the 1D operations in sum factorization into half [26, 38].

4.2 Data access

The data access when computing all cell and face integrals according to (1) with a matrix-free algorithm is shown in Figure 3. From the figure, it is apparent that the proposed basis minimizes the width of the effective “element-stencil”, only using one degree of freedom for the values and one for derivatives in face-normal direction, respectively. Accumulating the access of an element, the proposed Hermite-like basis reads $[(p + 1)^d + 4d(p + 1)^{d-1}]$ words, compared with $(2d + 1)(p + 1)^d$ reads for a conventional nodal basis. On general (curvilinear) element shapes, some geometric

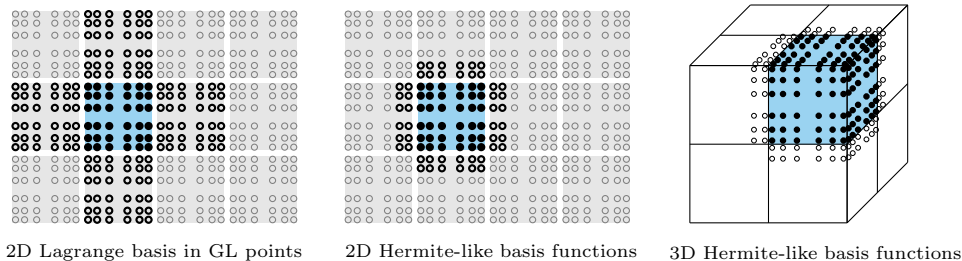


Figure 3: Data access pattern for $p = 5$ in terms of values read (black circles) for the element shaded in blue and values read and written (black disks). Note that the Hermite-like basis is not nodal and the two layers of nodes closest to the surface are highlighted for illustration purposes.

information must also be loaded. Computing a tri-linear mapping adds only little memory transfer for $p \geq 3$ and is of high arithmetic intensity. Isoparametric representations access $d(p+1)^d$ words per element and significantly increase both the data transfer and the arithmetic work.¹ To avoid computations, a separate Jacobian matrix \mathcal{J}_K^{-T} can be stored for each quadrature point of the cell and $\hat{n}^T \mathcal{J}_K^{-T}$ for each point on both sides of the faces, for a total of $d^2(p+1)^d + 4d^2(p+1)^{d-1}$ words per element [26]. Ignoring possible caching for neighboring vector entries, the proposed Hermite-like basis improves data access by a ratio 1:7 ($= 1 + 2d$) in the limit of large p when done on a 3D affine mesh without big geometry data and by a ratio 10:16 on a deformed mesh with separate Jacobians for each quadrature point, or somewhere in between depending on the evaluation of the geometry. As some neighboring data can be cached, the difference is smaller in practice when run on CPUs. As will be shown in the next section, the difference is significant nonetheless. For a GPU implementation, usually no neighbor data is cached and the improvement would be more significant.

5 Efficiency of matrix-free operator evaluation

In order to characterize the matrix-free operator evaluation with the proposed basis, we consider a 3D benchmark test of the Laplace operator with homogeneous Dirichlet boundary conditions. We construct an affine geometry by deforming the brick $(-0.95, 0.95) \times (-0.9, 0.89) \times (-0.85, 0.83)$ through a linear transformation with the Jacobian

$$\mathcal{J} = \begin{pmatrix} 1.12 & 0.24 & 0.36 \\ 0.24 & 1.36 & 0.48 \\ 0.36 & 0.48 & 1.60 \end{pmatrix}.$$

As mentioned above, we perform integration as if the geometry were deformed, but using the same merged tensor $\mathcal{J}_K^{-1} \mathcal{J}_K^{-T} \det(\mathcal{J}_K)$ in all points. This setup reduces the memory access besides the source and destination vectors to a minimum since the merged tensor resides in the cache at all times and thus better shows the effect of the basis. We create a mesh with $2^{l_1} 2^{l_2} 2^{l_3}$ hexahedral elements and a difference in mesh size of at most two, i.e., from the mesh sequence $1 \times 1 \times 1$, $2 \times 1 \times 1$, $2 \times 2 \times 1$, $2 \times 2 \times 2$, $4 \times 2 \times 2$, \dots . The mesh is selected depending on the polynomial degree to create a problem which has between 30 million and 56 million unknowns. This size makes sure that the vectors are much larger than the caches of a single node of the two processors listed in Table 2. Table 3 lists the meshes chosen for each degree.

The number of arithmetic operations per unknown for a matrix-vector product in the given setup is listed in Table 4 for the proposed Hermite-like basis as well as two nodal bases, a generic one based on the Gauss-Lobatto node points as well as the collocation case where the nodal points coincide with the quadrature points and $S = I$ in equations (4) and (5), which reduces the number of arithmetic operations. All sum factorization sweeps make use of the even-odd decomposition [38]. The ideal data access is 24 Bytes per DoF (3 doubles per DoF) for bases,

¹We note that the Hermite-like basis could also be used to reduce the data access when evaluating the metric terms \mathcal{J}_K on neighbors.

Table 2: Specification of hardware systems used for evaluation with turbo mode enabled on both. Memory bandwidth is according to the STREAM triad benchmark (optimized variant without read for ownership transfer involving two reads and one write) and GFLOP/s are based on the theoretical maximum at the AVX-512 frequency. The `dgemm` performance is measured for $m = n = k = 12,000$ with Intel MKL 18.0.2. The processor Xeon Platinum 8174 is a special model for SuperMUC-NG and not listed in official Intel documents. We measured a frequency of 2.7 GHz with AVX-512 dense code for the current experiments. The empirical machine balance is computed as the ratio of measured `dgemm` performance and STREAM bandwidth from RAM memory.

	Intel Cascade Lake Xeon Gold 6230	Intel Skylake Xeon Platinum 8174
cores	2×20	2×24
frequency base	2.1 GHz	2.7 GHz
max AVX-512 frequency	2.0 GHz	2.7 GHz
SIMD width	512 bit	512 bit
arithmetic peak	2560 GFLOP/s	4147 GFLOP/s
<code>dgemm</code> performance	2124 GFLOP/s	2920 GFLOP/s
memory interface	DDR4-2933, 12 channels	DDR4-2666, 12 channels
STREAM memory bandwidth	181 GB/s	205 GB/s
empirical machine balance	11.7 FLOP/Byte	14.3 FLOP/Byte
compiler	g++, version 9.1.0	
compiler flags	-O3 -funroll-loops -march=skylake-avx512	

Table 3: Number of elements $2^{l_1}2^{l_2}2^{l_3}$ and unknowns for different polynomial degrees.

degree p	1	2	3	4	5	6	7	8	9	10	11	12	13	14	15	16
$l_1 + l_2 + l_3$	22	21	19	18	18	17	16	16	15	15	15	14	14	14	13	13
n_{DoF}	34M	57M	34M	33M	57M	45M	34M	48M	33M	44M	57M	36M	45M	55M	34M	40M

one double to load the input vector, one double to write to the output vector, and an additional load operation on the output vector due to the read-for-ownership (RFO) data transfer [18]. Thus, the arithmetic intensity is between 8 and 14 FLOP/Byte for the Hermite-like basis and between 7 and 9.5 FLOP/Byte for the collocated nodal basis. Compared to the empirical machine balance of 11.7 FLOP/Byte of the Xeon Gold and 14.3 FLOP/Byte of Xeon Platinum, the roofline model [43] suggests that the algorithm is in a regime where both memory transfer and arithmetic matter. The particular instruction mix with the even-odd decomposition and operations at quadrature points yields an achievable floating point throughput of around 60–75% of peak for $p \leq 10$ due to the proportion of FMA instructions among all arithmetic instructions [26, Figure 3]. The effective machine balance on the Xeon Gold is hence around 7–8 FLOP/Byte and 10–11 FLOP/Byte on the Xeon Platinum. Assuming ideal execution, we expect the Xeon Gold to be core limited and the Xeon Platinum to be primarily memory access limited.

Our implementation² is based on the `deal.II` finite element library [3] and traverses the elements in the mesh in the Morton order (Z-order). In all experiments, vectorization over several elements is chosen according to [26], which yields batches of eight elements for double precision arithmetic and sixteen elements for single-precision arithmetic. For the given structured meshes, the Morton cell traversal ensures that a brick of closely packed elements are batched together. De-

²The code for all experiments is available on <https://github.com/kronbichler/multigrid>, subfolder `matvec_dg` for section 5 and `poisson_dg_plain`, `matvec_dg_cheby` for section 6, respectively.

Table 4: Number of arithmetic operations per degree of freedom (FLOP/DoF) for evaluating the 3D Laplacian with element-wise face integrals for the Hermite-like basis and nodal bases in Gauss–Lobatto points and Gauss points, respectively. Gaussian quadrature with $(p + 1)^3$ points is used. The numbers are based on counting the number of 1D interpolations times the cost of one interpolation per element, plus the work at quadrature points, and dividing by the unknowns per element.

polynomial degree p	1	2	3	4	5	7	9	11	16
Hermite-like basis	244	191	218	206	225	241	260	281	333
nodal Gauss–Lobatto basis	258	210	240	229	250	267	287	308	361
nodal Gauss basis	204	168	180	171	180	186	194	204	229

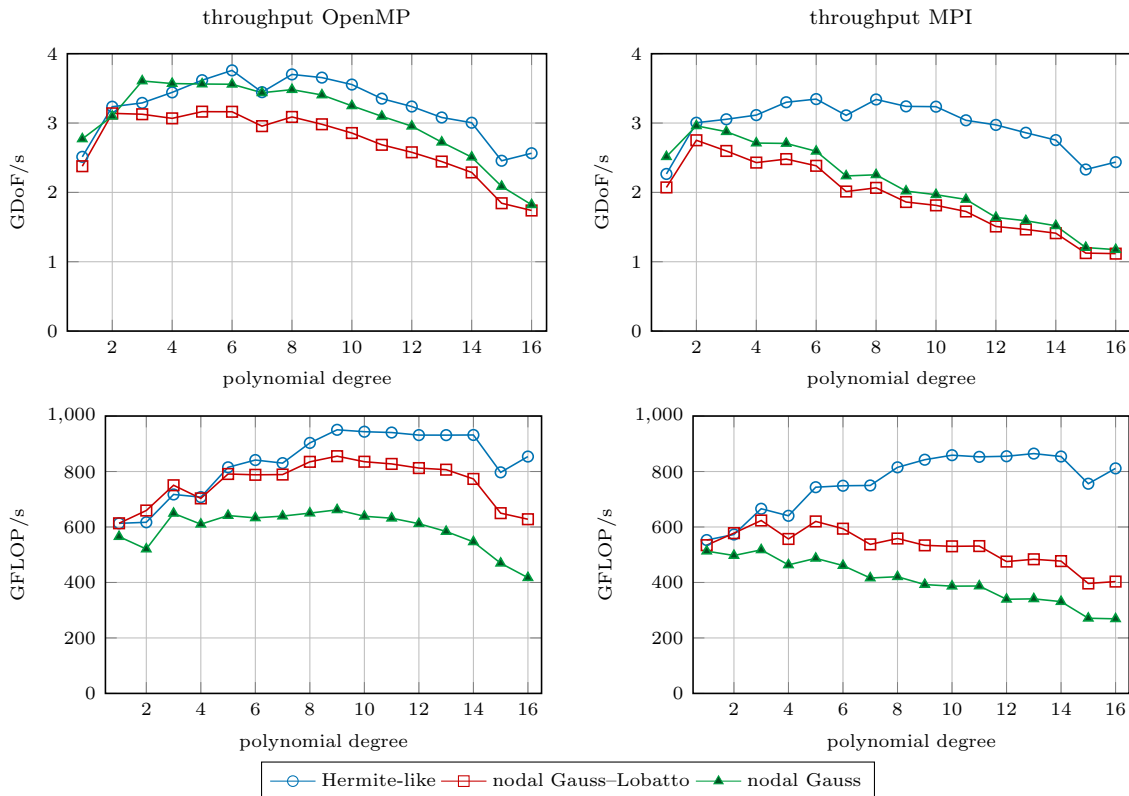


Figure 4: Throughput of double-precision matrix-vector product for the 3D Laplacian on an affine geometry in billion DoF/s for various bases with OpenMP (left panels) and MPI parallelization (right panels), respectively, on 2×20 Xeon Gold cores.

degrees of freedom are arranged cell-wise for easier implementation of multigrid solvers and mixed-precision algorithms using the same unknown numbering. Due to vectorization over cells, this involves transpose operations within SIMD lanes (array-of-struct to struct-of-array) at the beginning and the end of the cell access. We use a pure MPI parallelization with as many ranks as there are cores in the system (no hyperthreading), with parallel partitioning of the elements created by the `p4est` library via the Morton curve [6, 8]. The evaluation of face integrals requires exchange of data on elements which have a neighbor that is owned by another process. For the Hermite-like basis, we only need to exchange the $2(p+1)^{d-1}$ data items per face with ghost neighbor as given by the access highlighted in Figure 3, whereas the full ghosted elements are exchanged for the two nodal bases. In addition, a pure shared-memory parallelization based on OpenMP is considered, where the loop over element batches is split statically into as many partitions as there are threads resulting in a similar partitioning as in the MPI case. Threads are pinned to cores with the “close” affinity rule.

For the performance measurements, we record timings T for $n_{\text{tests}} = 200$ matrix-vector products for $p = 1, \dots, 16$ and report the throughput

$$\text{billion DoF / s} = \text{GDoF / s} = 10^{-9} \frac{n_{\text{tests}} n_{\text{DoF}}}{T}, \quad (10)$$

as common in this context [15]. We repeat the experiment 40 times and report the maximum throughput among those experiments. The standard deviation is 1–3%, mostly caused by background work of the operating system and the dynamic frequency adjustment of the processors. Figure 4 reports the results with the three bases on the Intel Xeon Gold Cascade Lake for the OpenMP and MPI parallelizations, respectively. The top two panels display the application throughput, whereas the bottom two panels the achieved floating point performance computed from the throughput in DoF/s multiplied by the work per unknown from Table 4. The OpenMP results show a similar arithmetic performance for the Hermite-like basis and the nodal Gauss–

Lobatto basis for degrees $p \leq 7$, indicating that both are primarily core-limited. Due to the cheaper face-normal interpolation via equation (5), the Hermite-like basis reaches a higher DoF/s throughput. The collocated nodal basis using Gauss points with less arithmetic work can initially outperform the other two bases in terms of GDoF/s. For higher polynomial degrees, $p \geq 5$, the proposed Hermite-like basis is the fastest variant with up to 20% advantage over the nodal Gauss basis. This result contradicts intuition in spectral element methods where collocated bases are favored, and underlines the importance of data access, even on a system like the Xeon Gold that tends to be core-limited.

When turning to the performance with the MPI parallelization, the advantage of the proposed Hermite-like basis becomes much more significant, achieving e.g. 48% higher throughput than the nodal Gauss basis with $p = 8$. While the new basis is able to sustain an approximately constant DoF/s throughput analogously to the OpenMP parallelization, the throughput with the nodal bases clearly drops due to the cost of the MPI data exchange as explained below.

Further insight into the advantages of the Hermite-like basis is given by an analysis of the data transfer of the complete matrix-vector product over the various levels of the memory hierarchy on the Xeon Gold in Figure 5. The analysis is based on hardware performance counters measured with the LIKWID tool [40]. The transfer between the core and the main memory, indicated by lines with cross marks in the figure, should ideally amount to 3 doubles per DoF. The lowest recorded values are around 3.5 to 4 doubles per DoF. The excess transfer appears because not all neighboring data can be cached for elements at far temporal distance (given by the Morton traversal), an effect well-studied in the context of finite difference stencils [18]. The measured data transfer from main memory is around 100–120 GB/s and thus below the STREAM bandwidth, indicating that the execution within the core puts the primary limit on execution. However, we see that the nodal bases start to deviate from the ideal behavior of low degrees once $p > 5$. This indicates that access to all DoF of an element, rather than only two layers with the Hermite-like basis, is of significance and reduces the effectiveness of caches. The increase of the memory transfer in the case of the Hermite-like basis for $p = 15, 16$ indicates the threshold where the temporary scratch arrays to perform interpolations of sum factorization exceed the caches, and the cross-element vectorization should be replaced by intra-element vectorization [26]. The more beneficial data access of the proposed Hermite-like basis is also visible for the transfer between the L1 and L2 cache as well as the transfer between the L2 and L3 cache. Even though the difference is not tremendous for the OpenMP parallelization, the proposed basis allows to fit data of around two degrees higher in the same cache level compared to the nodal bases.

In the MPI case, the data transfer is significantly higher because the implementation must pack the data for transfer into a separate buffer and eventually perform a mem-copy operation from one process to the other, despite actually running in shared memory. Adding these operations up, and considering that the ghost data is almost as big as the locally owned part for $p = 16$, the transfer from main memory is more than doubled. While the Hermite-like basis involves a main memory transfer of around 4–4.5 double per DoF (increasing the data access by around 0.5 double/DoF over the OpenMP case), the transfer rises to 10 double/DoF for the two nodal bases for $p = 12$, for instance. We note that this transfer cannot be overlapped with the local computations as it is not happening over an Infiniband fabric but either in user code for pack/unpack or a big `memcpy` call of the MPI library. As a consequence, the execution stalls at around 130–140 GB/s with a mix of phases with 100 GB/s (computation phase—compare to the OpenMP parallelization) and others with 180 GB/s (under the assumption that data exchange is performed with full bandwidth measured with the STREAM benchmark).

The throughput on the Xeon Platinum is shown in Figure 6. Overall, the trend is very similar to the Xeon Gold. As opposed to the experiment on the Xeon Gold of Figure 4, the OpenMP experiment is run with 2-way hyperthreading which gives around 5% higher throughput for $1 \leq p \leq 10$ than running without. For very high degrees $p \geq 12$, the caches are strained more with hyperthreading and twice the number of local scratch arrays for sum factorization which eventually spill to the slow main memory, such that throughput is even lower than on the Xeon Gold for $p = 15, 16$. On the other hand, the MPI parallelization on the Xeon Platinum does not profit from hyperthreading even for low degrees, so it is not used. A notable difference to the Xeon Gold is that the nodal Gauss–Lobatto and nodal Gauss bases show a more similar performance on the Xeon Platinum, which is expected from the preliminary characterization in terms of roofline: While Xeon Gold is core-limited, the Xeon Platinum is more strongly limited by the available

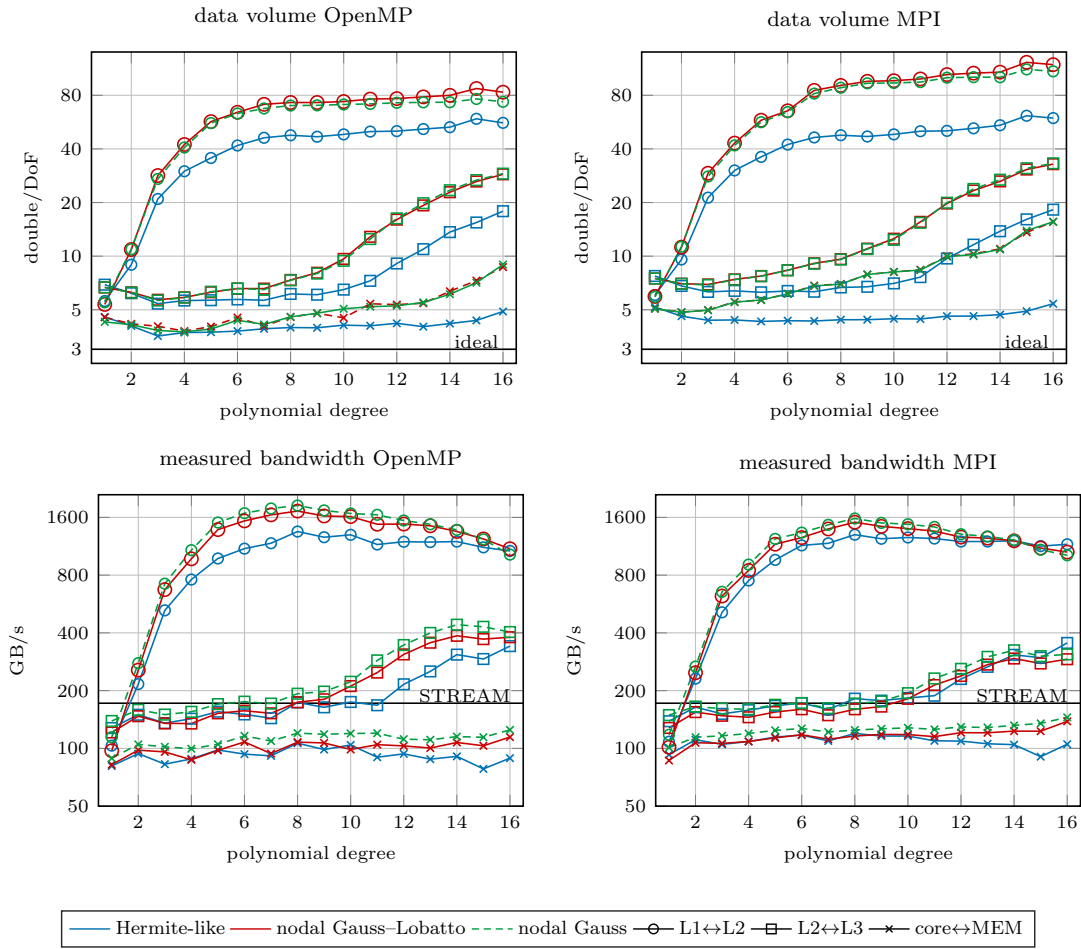


Figure 5: Analysis of data transfer over various memory hierarchies for executing the 3D DG-SIP Laplacian on 2×20 Xeon Gold cores.

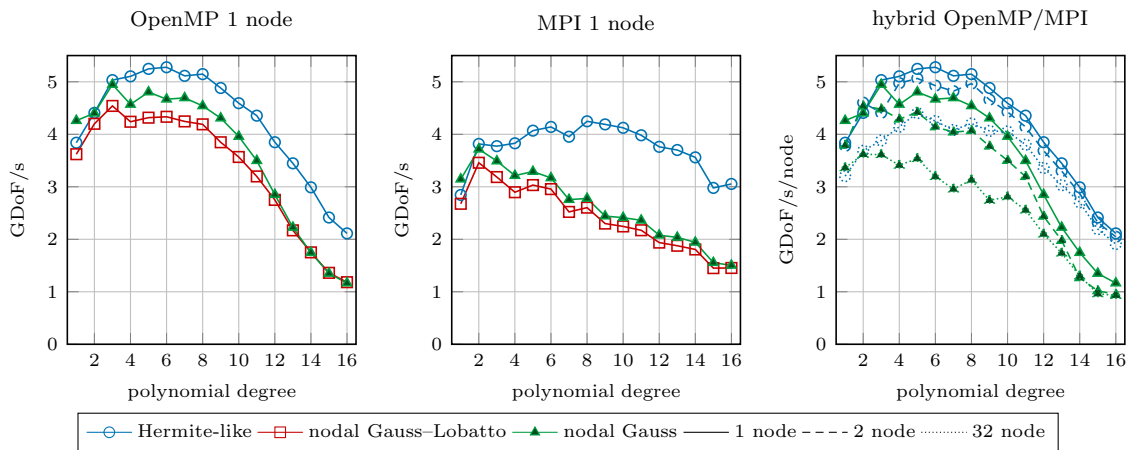


Figure 6: Throughput of double-precision matrix-vector product for the 3D Laplacian on an affine geometry in billion DoF/s for various bases with OpenMP and hyperthreading (left panel) and MPI parallelization (middle panel) on 1 node as well as up to 32 nodes with hybrid OpenMP/MPI (right panel), respectively, on 2×24 Xeon Platinum cores.

memory bandwidth. At the same time, the nodal Gauss–Lobatto and nodal Gauss bases have the same memory access pattern and only differ in the arithmetic work. With respect to arithmetic performance, we record up to 1.3 TFLOP/s on the Xeon Platinum (for polynomial degrees $p = 8, 9$), compared to 0.92 TFLOP/s on the Xeon Gold according to Figure 4. The measured memory throughput on the Xeon Platinum with the Hermite-like basis is up to 185 GB/s, or 127 GB/s in terms of theoretical throughput with 3 doubles per unknown. For the MPI case, the Xeon Platinum has less advantage over the Xeon Gold, which can be explained by the higher proportion of time spent in the memory-limited pack/unpack and MPI transfer routines.

The right panel of Figure 6 compares the throughput on one node with the throughput on 2 and 32 nodes of Xeon Platinum (using up to 1536 cores), respectively, in a weak scaling experiment. Here, the problem size per node is set to the data in Table 3, and the throughput per node is compared. Ideal weak scaling would correspond to coinciding curves for 1, 2, and 32 nodes. The performance degradation is expected because MPI pack/unpack operations must be included, bringing the observed performance closer to the MPI-only performance. In this setting, the proposed Hermite-like basis is able to maintain a much higher throughput than the nodal basis. This result confirms that large-scaling applications are behaving more like the MPI-only case, where the proposed basis has a significant advantage.

6 Application to multigrid

For explicit time integration, the results in section 5 directly translate to application performance. For implicit solvers, the matrix-vector product is embedded into some iterative solver. In this section, we analyze the effect of the basis on the throughput of a geometric multigrid solver using point-based smoothers and cell-based block Jacobi smoothers.

6.1 Algorithm

Multigrid methods are highly efficient and scalable solvers for the linear systems originating from elliptic partial differential equations. They combine simple iterative schemes, effective in removing the high-frequency content, on a hierarchy of coarser meshes. The hierarchy can be based on coarser meshes (geometric multigrid), on lower polynomial degrees (p -multigrid), or on algebraic coarsening based on the connectivity in the matrix (algebraic multigrid) [41]. The most expensive component of multigrid is usually the pre- and post-smoothing on the finest level. In a massively parallel context, the coarser level can contribute by the latency of the matrix-vector products [16, 29], a cost that is ignored here because it is mostly basis-agnostic.

For smoothing, a popular method in the context of matrix-free methods is the Chebyshev iteration [1] around a simple scheme, like the inverse of the matrix diagonal (point Jacobi) or some block-Jacobi/additive-Schwarz method with block size equal to the number of unknowns per element. The Chebyshev method is based on a three-term recurrence with iteration index j , computing the solution \mathbf{u}_{j+1} as follows,

$$\mathbf{u}_{j+1} = \mathbf{u}_j + \sigma_j(\mathbf{u}_j - \mathbf{u}_{j-1}) + \theta_j P^{-1}(\mathbf{b} - A\mathbf{u}_j), \quad (11)$$

where σ_j, θ_j are two scalar coefficients determined from Chebyshev polynomials [1], P^{-1} is the inner preconditioner (e.g., point Jacobi), \mathbf{b} is the right hand side of the linear system, and A the system matrix. The iteration is started with an initial guess \mathbf{u}_0 for the solution, e.g., from previous multigrid iterations or the coarse grid correction, and $\sigma_0 = 0$. The main computational expense in this method is the matrix-vector product, the application of the preconditioner, and some vector updates.

6.2 Efficiency with point-Jacobi/Chebyshev smoothing

The simplest choice for the Chebyshev iteration is the point-Jacobi scheme with $P = \text{diag}(A)$ in (11). As the quality of the point-Jacobi method strongly depends on the basis, this setup illustrates the properties of the Hermite-like basis. We solve the 3D Poisson equation on a cube $(-1, a_1) \times (-1, a_2) \times (-1, a_3)$ with refinement selection and number of unknowns as in Table 3. As before, we run the implementation for a general geometry and use a fixed geometric coefficient

Table 5: 3D Laplacian on a cube with MPI-only parallelization on 40 Xeon Gold cores: Number of conjugate gradient iterations n_9 to reduce the l_2 residual by 10^9 using geometric multigrid preconditioning with smoothing by a Chebyshev iteration of point-Jacobi (first three column groups) as well as a Chebyshev iteration with block-Jacobi via the fast diagonalization method (FDM) [32] according to section 6.4. The degree of the Chebyshev polynomial is 5 for both pre- and post-smoothing (i.e., 5 matrix-vector products).

basis P^{-1} p	Hermite-like point Jacobi			nodal Gauss–Lob.			nodal Gauss point Jacobi			Hermite-like block Jacobi: FDM		
	n_9	ρ	MDoF/s	n_9	ρ	MDoF/s	n_9	ρ	MDoF/s	n_9	ρ	MDoF/s
1	8	0.058	26.3	8	0.058	26.4	8	0.060	29.2	7	0.042	29.7
2	26	0.45	8.99	7	0.036	30.0	9	0.085	24.7	7	0.034	33.1
3	29	0.48	8.77	7	0.047	33.2	11	0.13	23.0	7	0.044	36.1
4	16	0.27	16.6	7	0.038	32.2	12	0.17	20.2	7	0.035	37.6
5	13	0.20	21.1	8	0.057	28.1	15	0.24	15.5	7	0.051	38.1
6	12	0.17	22.4	7	0.051	30.0	16	0.27	13.8	7	0.046	37.3
7	13	0.20	19.3	9	0.085	19.3	20	0.34	9.13	8	0.068	30.3
8	14	0.22	18.9	9	0.085	18.9	21	0.35	8.42	8	0.076	31.8
9	15	0.23	17.0	10	0.12	15.3	24	0.42	6.58	9	0.086	27.7
10	15	0.24	16.9	10	0.11	15.2	25	0.43	6.24	9	0.091	27.2
11	16	0.26	14.7	12	0.16	12.0	29	0.48	5.12	10	0.12	23.0
12	16	0.27	11.6	12	0.16	9.83	29	0.48	3.73	10	0.11	18.9

for all quadrature points to highlight the cost of vector data access. The lengths a_i are chosen to ensure cuboidal elements depending on the values of the mesh refinement l_1, l_2, l_3 . If $l_1 = l_2 = l_3$, we set $a_1 = a_2 = a_3 = 1$. If $l_1 = l_2 + 1 = l_3 + 1$, we set $a_1 = 3, a_2 = a_3 = 1$. Finally, if $l_1 = l_2 = l_3 + 1$, we set $a_1 = a_2 = 3, a_3 = 1$. The right hand side is chosen such that the solution satisfies $u(x, y, z) = \sin(3\pi x) \sin(3\pi y) \sin(3\pi z)$. Homogeneous Dirichlet conditions are set on all boundaries. We run a conjugate gradient solver preconditioned by a geometric multigrid V-cycle until the unpreconditioned l_2 norm of the residual, $\|\mathbf{b} - \mathbf{A}\mathbf{u}\|_2$, measured by residual estimate of the conjugate gradient method, has been reduced by 10^9 compared to the initial residual $\|\mathbf{b}\|_2$ with $\mathbf{u}^{(0)} = \mathbf{0}$. The multigrid V-cycle is completely done in single precision, whereas the conjugate gradient solver runs in double precision. This gives essentially identical accuracy as running the preconditioner in double precision but with almost twice the throughput, see also [17, 27]. On each level, pre- and postsmoothing is done with a Chebyshev smoother of degree 5. The relatively high degree is selected because it minimizes the time to solution with a nodal Gauss–Lobatto basis over a range of polynomial degrees between 1 and 12 for the given mixed-precision setup. The Chebyshev parameters are selected to smoothen components in the range $[0.06\tilde{\lambda}_{\max}, 1.2\tilde{\lambda}_{\max}]$ which is robust also for mildly variable coefficients [27]. Here, $\tilde{\lambda}_{\max}$ is an estimate of the largest eigenvalues found by 15 Lanczos iterations, starting with the vector $[-5.5, -4.5, \dots, 4.5, 5.5, -5.5, -4.5, \dots]$. As a coarse-grid solver, we use the Chebyshev iteration with the degree such that the a-priori error estimate of the Chebyshev iteration guarantees a residual reduction by at least 10^5 [42].

The results of the multigrid experiment for polynomial degrees $1 \leq p \leq 12$ are presented in Table 5. Both the number of iterations n_9 and the multigrid convergence rate $\rho = (\|\mathbf{r}_{n_9}\|_2 / \|\mathbf{r}_0\|_2)^{1/n_9}$, involving the initial unpreconditioned residual $\mathbf{r}_0 = \mathbf{b}$ and the residual \mathbf{r}_{n_9} after n_9 iterations, are given. Furthermore, the table presents the throughput of the multigrid solver in terms of million degrees of freedom solved per second (MDoF/s), computed as the number of unknowns from Table 3 divided by the run time of the solver with an MPI-only parallelization. The table compares the Hermite-like basis with a nodal Gauss–Lobatto basis and a nodal Gauss basis for a point-Jacobi representation of P^{-1} in equation (11) as well as block-Jacobi variant described in Section 6.4 below. Among the three bases, the nodal Gauss–Lobatto basis gives the best multigrid performance with point Jacobi and, as a result, the highest solver throughput for $p \leq 6$. In other words, even though the Hermite-like basis provides the fastest matrix-vector product according to the right panel of Figure 4, a simple point-Jacobi smoother counteracts these benefits due to more multigrid iterations. The nodal Gauss basis leads to relatively high iteration counts, showing that optimality with respect to the mass matrix (which is diagonal in the collocated Gauss case) does not translate to good performance for smoothing with the Laplacian. This also means that the Hermite basis could be somewhat improved by using the additional degrees of freedom for orthogonality with respect to the discrete Laplacian.

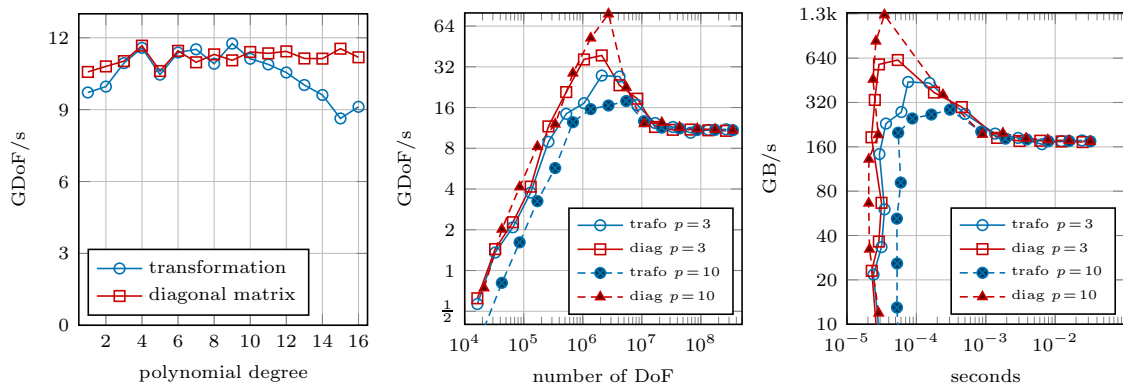


Figure 7: Analysis of evaluation of operator P^{-1} with basis transformation (12) versus a diagonal representation as function of the degree with 30–56 million DoF (left panel), as function of the size (middle panel), and as function of the evaluation time (right panel). The middle and right panels use the same data. All operations are done in single precision and with OpenMP on Xeon Gold.

6.3 Evaluation of P^{-1}

A more general approach to remedy the disadvantage of the Hermite-like basis with point-Jacobi smoothing is a change of basis, which can recover the behavior of any other DG basis. To achieve this, we consider a preconditioner P in the Chebyshev iteration (11) constructed as

$$\left(P^{(K)}\right)^{-1} = \left(T^{\top} \otimes T^{\top} \otimes T^{\top}\right) \left(\hat{P}_d^{(K)}\right)^{-1} \left(T \otimes T \otimes T\right), \quad (12)$$

where $\hat{P}_d^{(K)}$ is an element-wise diagonal matrix. The matrix T is some reference-cell 1D transformation matrix. For example, a change into the nodal Gauss–Lobatto basis for the sake of applying a diagonal operator \hat{P}_d^{-1} allows the Hermite-like basis to run with the same iteration counts as the nodal Gauss–Lobatto basis (not shown) but with a considerably faster matrix-vector product. For $p = 7$, the nodal Gauss–Lobatto basis with a point-Jacobi smoother solves 19.3 MDoF/s on 40 cores, whereas the Hermite-like basis including the transformation (12) to the Gauss–Lobatto basis solves 26.7 MDoF/s.

To understand why the basis change leads to an increase in performance despite additional arithmetic work, Figure 7 compares the throughput of P^{-1} with the basis change (12) against the application of a diagonal matrix (i.e., vector scaling) for experiments in single precision. The throughput for large sizes is essentially the same for both variants because they are both bound by the memory bandwidth of reading the vectors for $p \leq 11$, confirming previous results for the inverse mass matrix evaluation in [13, 37] which is the same operation from an implementation point view [28]. In this experiment, $4 \times 4 = 16$ Byte/DoF must be accessed (read input & diagonal, write and RFO for output), for 20–50 FLOP/DoF for $1 \leq p \leq 7$. For very high degrees, there is a slight degradation in throughput for the transformation as the arithmetic work becomes notable. Experiments that vary the size of the problem are shown in the middle and right panels of Figure 7. For an intermediate regime with enough parallelism on the one hand and all data in the L2 and L3 caches on the other hand, the diagonal preconditioner is faster as expected. However, the transformed variant also runs much faster when vectors are in cache, e.g., with 440 GB/s for $p = 3$ compared to the saturated performance of 180 GB/s. The in-cache case where the diagonal matrix is advantageous is actually narrow: It only matters when the time per iteration including the matrix-vector is around 0.5 milliseconds or less. However, this regime is often beyond the strong scaling limit [15] where the network latency in the matrix-vector products on various levels is the dominant cost.

6.4 Choice of inner preconditioner for Hermite-like basis

The transformation from the Hermite-like basis into the nodal Gauss–Lobatto basis for the purpose of smoothing is not the best one can do with formula (12). On a Cartesian (axis-aligned) mesh

and with constant coefficients, the tensor structure of shape functions and quadrature formula propagates into the final cell matrix. Therefore, the discretization of the scalar Laplacian admits an exact block-Jacobi preconditioner of the form (12), where each block coincides with the cell-wise homogeneous problem (1).

For example, applying $\det(\mathcal{J}_K) = h^3$ and $\mathcal{J}_K^{-1} = \text{diag}(h^{-1}, h^{-1}, h^{-1})$, where h is the characteristic length of the Cartesian cell K , to the cell term (3) with the ansatz function $u_h = \varphi_j$ it follows

$$(\nabla\varphi_i, \nabla\varphi_j)_K = \sum_{t=1}^3 \left(\int_0^1 \frac{1}{h} \phi'_{it} \phi'_{jt} d\xi_t \prod_{\tau=1, \tau \neq t}^3 \int_0^1 h \phi_{i\tau} \phi_{j\tau} d\xi_\tau \right). \quad (13)$$

The associated stiffness matrix is a three-termed sum of Kronecker products of the one-dimensional stiffness and mass matrices. Proceeding similarly with the face integrals of the DG discretization, the matrix A_K corresponding to (1) has the form

$$A^{(K)} = M \otimes M \otimes L_{\text{DG}} + M \otimes L_{\text{DG}} \otimes M + L_{\text{DG}} \otimes M \otimes M, \quad (14)$$

where L_{DG} represents the stiffness matrix of the 1D discretization of (1) and M the mass matrix on an interval with length h . The generalized symmetric definite eigenproblem of the form $L_{\text{DG}}\mathbf{z} = \lambda M\mathbf{z}$ naturally leads to a basis transformation of $(A^{(K)})^{-1}$ of the form (12) [31, 32]. Here, the transformation matrix T is the column-wise concatenation of generalized eigenvectors \mathbf{z} and the element-wise diagonal matrix is

$$\left(\hat{P}_d^{(K)}\right)^{-1} = (I \otimes I \otimes \Lambda + I \otimes \Lambda \otimes I + \Lambda \otimes I \otimes I)^{-1}, \quad (15)$$

where the diagonal matrix Λ contains the generalized eigenvalues λ and I is the identity matrix. Consequently, the tensor structure of the DG discretization of the scalar Laplacian admits an exact element-wise preconditioner with diagonal form independent of the choice of the polynomial basis. The inverse of $A^{(K)}$ in (14) is efficiently computed in terms of the fast diagonalization method (FDM) [32]. We note that (14) needs to be slightly modified for elements at the boundary due to the different weights resulting from the mirror principle. In this work, we neglect this fact and use an approximate variant (14) with matrices from interior elements everywhere. For further details on such block-based smoothers and possible extensions to non-Cartesian meshes, see [44].

The last three columns of Table 5 report the iteration counts and run time with an FDM-based representation in equation (12). While the basis shows similar iteration counts as the nodal Gauss–Lobatto case for $p \leq 4$, its multigrid convergence rates are better for higher degrees. As explained above, combined with the basis change in the smoother (12) the Hermite-like basis offers the best performance in terms of time to solution.

6.5 Efficiency of Chebyshev iteration

Due to the high performance of the matrix-vector product, which is within a factor of 1.7 in throughput to simply copying the involved vectors, the vector updates in the Chebyshev update formula (11) become critical. For optimal performance, they must be merged with the other operations as much as possible. Also, the isolated consideration of P^{-1} as in Figure 7 is not enough. In this section, we study two variants. The first variant, labeled “separate”, computes $A\mathbf{u}^{(j)}$ and stores it in a temporary vector. In a second loop through the data, the temporary vector is read again, P^{-1} is applied, and combined with the vectors. If P^{-1} is represented by a vector (inverse diagonal), this approach accesses 3 words of memory per unknown for the matrix-vector product (including RFO) and 6 words during the preconditioner evaluation and vector update phase, namely reading from \mathbf{b} , $A\mathbf{u}^{(j)}$, \hat{P}_d^{-1} , $\mathbf{u}^{(j-1)}$, $\mathbf{u}^{(j)}$, as well as writing the result $\mathbf{u}^{(j+1)}$ back into the storage location of $\mathbf{u}^{(j-1)}$ (this avoids the RFO transfer). The second variant, labeled “merged”, makes use of the fact that the matrix-vector product computes the full result on an element within a single sweep. Thus, after finishing the matrix-vector product on an element, we immediately compute the residual, apply P^{-1} , and add the vector contributions. In this variant, the temporary results as well as $\mathbf{u}^{(j)}$ are still hot in caches, leading to a best-case data access of 5 words per unknown. All results in Table 5 are based on the faster fully merged variant.

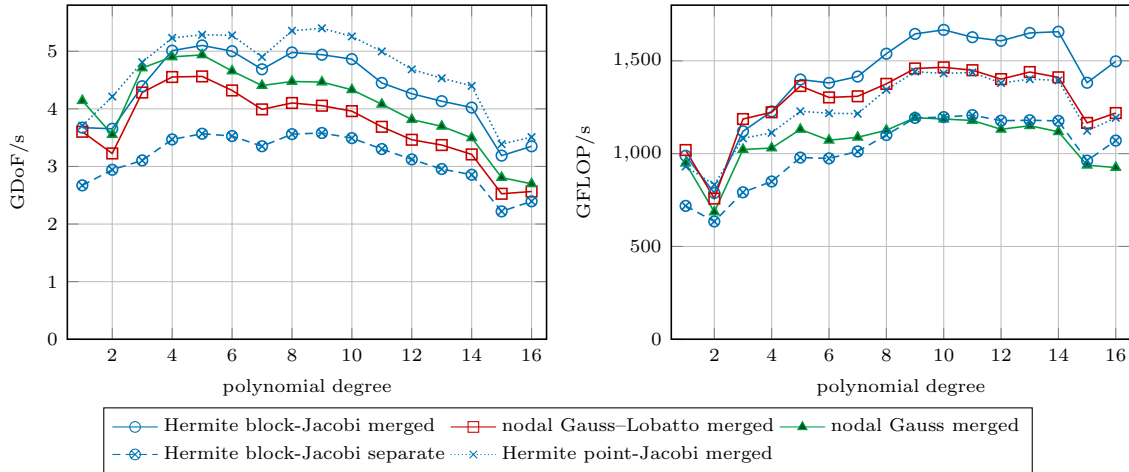


Figure 8: Throughput of one step within single-precision Chebyshev iteration ($j > 0$) with the 3D Laplacian on an affine geometry for various bases with OpenMP parallelization on 2×20 Xeon Gold cores. Both a block-Jacobi and diagonal preconditioner P^{-1} are considered as well as separate matrix-vector product and fully merged iteration.

Figure 8 reports the throughput of one step in the Chebyshev iteration (11) when run for a generic index $j > 0$ (i.e., $\mathbf{u}^{(j-1)}$ must be accessed) in single precision. The fully merged variant is considerably faster due to the lower vector access, reaching 5.0 GDoF/s per iteration for $p = 8$ versus 3.6 GDoF/s when the matrix-vector product runs separately. Note that the measured memory transfer of 120 GB/s is around 30 GB/s less for the merged case and not fully utilizing the memory interface.

When it comes to a point-Jacobi versus a block-Jacobi variant according to (12), Figure 8 confirms that the basis change is almost for free. As opposed to Figure 7 or when run with a slower separate matrix-vector product, there is a small gap in throughput with the fastest implementation also for $p < 12$ because the overall merged operator is not fully memory limited. Nonetheless, the experiment is encouraging from a mathematical point of view because it allows to select a basis where the diagonal is a good smoother: The arithmetic operations for the basis change can mostly be hidden behind the memory transfer in the Chebyshev loop also on an architecture with a relatively low machine balance. The difference between the diagonal and block-diagonal setup is even smaller on the Xeon Platinum with more FLOP/Byte.

7 Conclusions

We have presented a Hermite-like basis that enables faster matrix-free evaluation of symmetric interior penalty DG discretizations of the Laplacian but at the same time yields the same results as a nodal Lagrangian basis due to consistent integration. As opposed to the higher-order continuity typically associated with Hermite polynomials, our approach targets the fully discontinuous L_2 -conforming case and is motivated by the favorable data access. We have shown that the basis significantly reduces the amount of vector data access on neighbors for higher degree polynomials and especially with an MPI-only parallelization. Furthermore, caches become more effective in holding neighbor data. We have shown an 8–20% increase in performance over nodal bases for an OpenMP parallelization and up to $2\times$ higher performance with an MPI parallelization for polynomial degrees between 5 and 10. The basis is specifically designed for modern hardware with high FLOP/Byte ratios, i.e., where data access is expensive as compared to computations.

The proposed basis relies on a combination of the Hermite polynomials with nodal polynomials based on roots of Jacobi polynomials to ensure a well-conditioned interpolation. While the basis is not interpolatory, it is constructed such that optimizations of nodal codes like the even-odd decomposition are applicable. Using the proposed basis with a point-Jacobi smoother in a multigrid solver leads to worse behavior than with nodal Lagrange polynomials based on Gauss-Lobatto points. We have therefore proposed to combine fast operator evaluation in the Hermite-like basis

with a basis change into a more favorable basis for preconditioning. This basis could be the nodal Gauss–Lobatto one, but more beneficial ones as exemplified by the basis spanned by generalized eigenvectors from the fast diagonalization method are also possible. The change of basis happens in an otherwise memory-bandwidth limited algorithm and can therefore be almost completely hidden behind the cost of memory transfer.

Acknowledgments

The authors thank Anian Fuchs and Guido Kanschat for discussions about implementation aspects for the Hermite basis functions.

A Explicit formula of Hermite-like polynomials

Basis functions for $p = 2$:

$$\phi_0(\xi) = (1 - \xi)^2, \quad \phi_1(\xi) = 2\xi(1 - \xi), \quad \phi_2(\xi) = \xi^2.$$

Basis functions for $p = 3$:

$$\begin{aligned} \phi_0(\xi) &= -\frac{7}{2} \left(\xi - \frac{2}{7} \right) (\xi - 1)^2, & \phi_1(\xi) &= \frac{11}{2} \xi (\xi - 1)^2, \\ \phi_2(\xi) &= -\frac{11}{2} \xi^2 (\xi - 1), & \phi_3(\xi) &= \frac{7}{2} \xi^2 \left(\xi - \frac{5}{7} \right). \end{aligned}$$

Basis functions for $p = 4$:

$$\begin{aligned} \phi_0(\xi) &= 12 \left(\xi - \frac{1}{6} \right) \left(\xi - \frac{1}{2} \right) (\xi - 1)^2, & \phi_1(\xi) &= -20\xi \left(\xi - \frac{1}{2} \right) (\xi - 1)^2, \\ \phi_2(\xi) &= 16\xi^2 (\xi - 1)^2, \\ \phi_3(\xi) &= -20\xi^2 \left(\xi - \frac{1}{2} \right) (\xi - 1), & \phi_4(\xi) &= 12\xi^2 \left(\xi - \frac{1}{2} \right) \left(\xi - \frac{5}{6} \right). \end{aligned}$$

Basis functions for $p = 5$:

$$\begin{aligned} \phi_0(\xi) &= -\frac{198}{5} \left(\xi - \frac{1}{9} \right) \left(\xi - \frac{1}{2} + \sqrt{\frac{1}{44}} \right) \left(\xi - \frac{1}{2} - \sqrt{\frac{1}{44}} \right) (\xi - 1)^2, \\ \phi_1(\xi) &= \frac{1694}{25} \xi \left(\xi - \frac{1}{2} + \sqrt{\frac{1}{44}} \right) \left(\xi - \frac{1}{2} - \sqrt{\frac{1}{44}} \right) (\xi - 1)^2, \\ \phi_2(\xi) &= -\frac{242\sqrt{44}}{25} \xi^2 \left(\xi - \frac{1}{2} - \sqrt{\frac{1}{44}} \right) (\xi - 1)^2, \\ \phi_3(\xi) &= \frac{242\sqrt{44}}{25} \xi^2 \left(\xi - \frac{1}{2} + \sqrt{\frac{1}{44}} \right) (\xi - 1)^2, \\ \phi_4(\xi) &= -\frac{1694}{25} \xi^2 \left(\xi - \frac{1}{2} + \sqrt{\frac{1}{44}} \right) \left(\xi - \frac{1}{2} - \sqrt{\frac{1}{44}} \right) (\xi - 1), \\ \phi_5(\xi) &= \frac{198}{5} \xi^2 \left(\xi - \frac{1}{2} + \sqrt{\frac{1}{44}} \right) \left(\xi - \frac{1}{2} - \sqrt{\frac{1}{44}} \right) \left(\xi - \frac{8}{9} \right). \end{aligned}$$

An algorithm for the polynomials for arbitrary order according to Section 4 is given in the deal.II library, version 9.0, class `HermiteLikeInterpolation`, <https://github.com/dealii/dealii/blob/dealii-9.0/source/base/polynomial.cc>, lines 1373–1494, retrieved on July 12, 2019.

References

- [1] M. ADAMS, M. BREZINA, J. HU, AND R. TUMINARO, *Parallel multigrid smoothing: polynomial versus Gauss–Seidel*, J. Comput. Phys., 188 (2003), pp. 593–610, doi:10.1016/S0021-9991(03)00194-3.
- [2] M. AINSWORTH, G. ANDRIAMARO, AND O. DAVYDOV, *Bernstein–Bézier finite elements of arbitrary order and optimal assembly procedures*, SIAM J. Sci. Comput., 33 (2011), pp. 3087–3109, doi:10.1137/11082539X.
- [3] G. ALZETTA, D. ARNDT, W. BANGERTH, V. BODDU, B. BRANDS, D. DAVYDOV, R. GASSMOELLER, T. HEISTER, L. HELTAI, K. KORMANN, M. KRONBICHLER, M. MAIER, J.-P. PELTERET, B. TURCK SIN, AND D. WELLS, *The deal.II library, version 9.0*, J. Numer. Math., 26 (2018), pp. 173–184, doi:10.1515/jnma-2018-0054, www.dealii.org.
- [4] D. APPELÖ, T. HAGSTROM, AND A. VARGAS, *Hermite methods for the scalar wave equation*, SIAM J. Sci. Comput., 40 (2018), pp. A3902–A3927, doi:10.1137/18M1171072.
- [5] D. ARNOLD, F. BREZZI, B. COCKBURN, AND L. D. MARINI, *Unified analysis of discontinuous Galerkin methods for elliptic problems*, SIAM J. Numer. Anal., 39 (2002), pp. 1749–1779, doi:10.1137/S0036142901384162.
- [6] W. BANGERTH, C. BURSTEDDE, T. HEISTER, AND M. KRONBICHLER, *Algorithms and data structures for massively parallel generic finite element codes*, ACM Trans. Math. Softw., 38 (2011), pp. 14:1–14:28, doi:10.1145/2049673.2049678.
- [7] S. BEUCHLER, V. PILLWEIN, AND S. ZAGLMAYR, *Sparsity optimized high order finite element functions for $H(\text{div})$ on simplices*, Numer. Math., 122 (2012), pp. 197–225, doi:10.1007/s00211-012-0461-0.
- [8] C. BURSTEDDE, L. C. WILCOX, AND O. GHATTAS, *p4est: Scalable algorithms for parallel adaptive mesh refinement on forests of octrees*, SIAM J. Sci. Comput., 33 (2011), pp. 1103–1133, doi:10.1137/10079163, <http://p4est.org>.
- [9] B. COCKBURN, J. GOPALAKRISHNAN, AND R. LAZAROV, *Unified hybridization of discontinuous Galerkin, mixed, and continuous Galerkin methods for second order elliptic equations*, SIAM J. Numer. Anal., 47 (2009), pp. 1139–1365, doi:10.1137/070706616.
- [10] A. CRIVELLINI AND F. BASSI, *An implicit matrix-free discontinuous Galerkin solver for viscous and turbulent aerodynamic simulations*, Comput. Fluids, 50 (2011), pp. 81–93, doi:10.1016/j.compfluid.2011.06.020.
- [11] M. O. DEVILLE, P. F. FISCHER, AND E. H. MUND, *High-order methods for incompressible fluid flow*, vol. 9, Cambridge University Press, 2002.
- [12] Y. EPSHTEYN AND B. RIVIÈRE, *Estimation of penalty parameters for symmetric interior penalty Galerkin methods*, J. Comput. Appl. Math., 206 (2007), pp. 843–872, doi:10.1016/j.cam.2006.08.029.
- [13] N. FEHN, W. A. WALL, AND M. KRONBICHLER, *Efficiency of high-performance discontinuous Galerkin spectral element methods for under-resolved turbulent incompressible flows*, Int. J. Numer. Meth. Fluids, 88 (2018), pp. 32–54, doi:10.1002/fld.4511.
- [14] N. FEHN, W. A. WALL, AND M. KRONBICHLER, *Robust and efficient discontinuous Galerkin methods for under-resolved turbulent incompressible flows*, J. Comput. Phys., 372 (2018), pp. 667–693, doi:10.1016/j.jcp.2018.06.037.
- [15] P. FISCHER, T. RATHNAYAKE, S. DUTTA, V. DOBREV, T. KOLEV, J.-S. CAMIER, M. KRONBICHLER, K. ŚWIRYDOWICZ, T. WARBURTON, J. BROWN, AND M. MIN, *Running faster in HPC applications*, in preparation, (2019). <http://ceed.exascaleproject.org>.
- [16] A. GHOLAMI, D. MALHOTRA, H. SUNDAR, AND G. BIROS, *FFT, FMM, or multigrid? A comparative study of state-of-the-art Poisson solvers for uniform and nonuniform grids in the unit cube*, SIAM J. Sci. Comput., 38 (2016), pp. C280–C306, doi:10.1137/15M1010798.
- [17] W. D. GROPP, D. K. KAUSHIK, D. E. KEYES, AND B. F. SMITH, *Performance modeling and tuning of an unstructured mesh CFD application*, in SC’00: Proceedings of the 2000 ACM/IEEE Conference on Supercomputing, 2000, pp. 34–34, doi:10.1109/SC.2000.10059.
- [18] G. HAGER AND G. WELLEIN, *Introduction to High Performance Computing for Scientists and Engineers*, CRC Press, Boca Raton, 2011.
- [19] P. W. HEMKER, W. HOFFMANN, AND M. H. VAN RAALTE, *Two-level Fourier analysis of a multigrid approach for discontinuous Galerkin discretization*, SIAM J. Sci. Comput., 25 (2003), pp. 1018–1041, doi:10.1137/S1064827502405100.
- [20] F. HINDENLANG, G. GASSNER, C. ALTMANN, A. BECK, M. STAUDENMAIER, AND C.-D. MUNZ, *Explicit discontinuous Galerkin methods for unsteady problems*, Comput. Fluids, 61 (2012), pp. 86–93, doi:10.1016/j.compfluid.2012.03.006.

- [21] I. HUISMANN, J. STILLER, AND J. FRÖHLICH, *Factorizing the factorization – a spectral-element solver for elliptic equations with linear operation count*, J. Comput. Phys., 346 (2017), pp. 437–448, doi:10.1016/j.jcp.2017.06.012.
- [22] R. C. KIRBY, *Fast inversion of the simplicial Bernstein mass matrix*, Numer. Math., 135 (2017), pp. 73–95, doi:10.1007/s00211-016-0795-0.
- [23] M. G. KNEPLEY, J. BROWN, K. RUPP, AND B. F. SMITH, *Achieving high performance with unified residual evaluation*, arXiv preprint cs.MS, 1309.1204 (2013), pp. 1–4.
- [24] D. KOPRIVA, *Implementing spectral methods for partial differential equations*, Springer, Berlin, 2009.
- [25] M. KRONBICHLER AND K. KORMANN, *A generic interface for parallel cell-based finite element operator application*, Comput. Fluids, 63 (2012), pp. 135–147, doi:10.1016/j.compfluid.2012.04.012.
- [26] M. KRONBICHLER AND K. KORMANN, *Fast matrix-free evaluation of discontinuous Galerkin finite element operators*, ACM Trans. Math. Softw., in press (2019), pp. 1–37, doi:10.1145/3325864.
- [27] M. KRONBICHLER AND K. LJUNGKVIST, *Multigrid for matrix-free high-order finite element computations on graphics processors*, ACM Trans. Parallel Comput., 6 (2019), pp. 2:1–2:32, doi:10.1145/3322813.
- [28] M. KRONBICHLER, S. SCHOEDER, C. MÜLLER, AND W. A. WALL, *Comparison of implicit and explicit hybridizable discontinuous Galerkin methods for the acoustic wave equation*, Int. J. Numer. Meth. Eng., 106 (2016), pp. 712–739, doi:10.1002/nme.5137.
- [29] M. KRONBICHLER AND W. A. WALL, *A performance comparison of continuous and discontinuous Galerkin methods with fast multigrid solvers*, SIAM J. Sci. Comput., 40 (2018), pp. A3423–A3448, doi:10.1137/16M110455X.
- [30] C. LEHRENFELD AND J. SCHÖBERL, *High order exactly divergence-free hybrid discontinuous Galerkin methods for unsteady incompressible flows*, Comput. Meth. Appl. Mech. Eng., 307 (2016), pp. 339–361, doi:10.1016/j.cma.2016.04.025.
- [31] J. W. LOTTES AND P. F. FISCHER, *Hybrid multigrid/Schwarz algorithms for the spectral element method*, J. Sci. Comput., 24 (2005), pp. 45–78, doi:10.1007/s10915-004-4787.
- [32] R. E. LYNCH, J. R. RICE, AND D. H. THOMAS, *Direct solution of partial difference equations by tensor product methods*, Numer. Math., 6 (1964), pp. 185–199, doi:10.1007/BF01386067.
- [33] S. A. ORSZAG, *Spectral methods for problems in complex geometries*, J. Comput. Phys., 37 (1980), pp. 70–92, doi:10.1016/0021-9991(80)90005-4.
- [34] J. PERAIRE AND P.-O. PERSSON, *The compact discontinuous Galerkin (CDG) method for elliptic problems*, SIAM J. Sci. Comput., 30 (2008), pp. 1806–1824, doi:10.1137/070685518.
- [35] P. PERSSON, *A sparse and high-order accurate line-based discontinuous Galerkin method for unstructured meshes*, J. Comput. Phys., (2013), pp. 414–429, doi:10.1016/j.jcp.2012.09.008.
- [36] M. PIATKOWSKI, S. MÜTHING, AND P. BASTIAN, *A stable and high-order accurate discontinuous Galerkin based splitting method for the incompressible Navier–Stokes equations*, J. Comput. Phys., 356 (2018), pp. 220–239, doi:10.1016/j.jcp.2017.11.035.
- [37] S. SCHOEDER, K. KORMANN, W. A. WALL, AND M. KRONBICHLER, *Efficient explicit time stepping of high order discontinuous Galerkin schemes for waves*, SIAM J. Sci. Comput., 40 (2018), pp. C803–C826, doi:10.1137/18M1185399.
- [38] A. SOLOMONOFF, *A fast algorithm for spectral differentiation*, J. Comput. Phys., 98 (1992), pp. 174–177, doi:10.1016/0021-9991(92)90182-X.
- [39] H. SUNDAR, G. STADLER, AND G. BIROS, *Comparison of multigrid algorithms for high-order continuous finite element discretizations*, Numer. Linear Algebra Appl., 22 (2015), pp. 664–680, doi:10.1002/nla.1979.
- [40] J. TREIBIG, G. HAGER, AND G. WELLEIN, *LIKWID: A lightweight performance-oriented tool suite for x86 multicore environments*, in Proceedings of PSTI2010, the First International Workshop on Parallel Software Tools and Tool Infrastructures, San Diego CA, 2010, doi:10.1109/ICPPW.2010.38. <https://github.com/RRZE-HPC/likwid>, retrieved on June 19, 2019.
- [41] U. TROTTEBERG, C. OOSTERLEE, AND A. SCHÜLLER, *Multigrid*, Elsevier Academic Press, London, 2001.
- [42] R. S. VARGA, *Matrix iterative analysis*, Springer, Berlin, 2nd ed., 2009.
- [43] S. WILLIAMS, A. WATERMAN, AND D. PATTERSON, *Roofline: An insightful visual performance model for multicore architectures*, Commun. ACM, 52 (2009), pp. 65–76, doi:10.1145/1498765.1498785.
- [44] J. WITTE, D. ARNDT, AND G. KANSCHAT, *Fast tensor product Schwarz smoothers*, 2019. in preparation.